RESEARCH ARTICLE

Stable Cuprous Hydroxide Nanostructures by Organic Ligand Functionalization

Qiming Liu, Yi Peng, Zaheer Masood, Davida DuBois, John Tressel, Forrest Nichols, Paul Ashby, Rene Mercado, Tufa Assafa, Dingjie Pan, Han-Lin Kuo, Jennifer Q. Lu, Frank Bridges, Glenn Millhauser, Qingfeng Ge,* and Shaowei Chen*

Copper compounds have been extensively investigated for diverse applications. However, studies of cuprous hydroxide (CuOH) have been scarce due to structural metastability. Herein, a facile, wet-chemistry procedure is reported for the preparation of stable CuOH nanostructures via deliberate functionalization with select organic ligands, such as acetylene and mercapto derivatives. The resulting nanostructures are found to exhibit a nanoribbon morphology consisting of small nanocrystals embedded within a largely amorphous nanosheet-like scaffold. The acetylene derivatives are found to anchor onto the CuOH forming Cu—C≡ linkages, whereas Cu—S— interfacial bonds are formed with the mercapto ligands. Effective electronic coupling occurs at the ligand-core interface in the former, in contrast to mostly non-conjugated interfacial bonds in the latter, as manifested in spectroscopic measurements and confirmed in theoretical studies based on first principles calculations. Notably, the acetylene-capped CuOH nanostructures exhibit markedly enhanced photodynamic activity in the inhibition of bacteria growth, as compared to the mercapto-capped counterparts due to a reduced material bandgap and effective photocatalytic generation of reactive oxygen species. Results from this study demonstrate that deliberate structural engineering with select organic ligands is an effective strategy in the stabilization and functionalization of CuOH nanostructures, a critical first step in exploring their diverse applications.

1. Introduction

Copper, as a multi-valence element, can form a wide range of compounds, including oxides,[1,2] hydroxides,[3,4] chalcogenides,[5,6] halides,[7,8] and some complicated salts (e.g., Chevreul's salt),[9] which have found diverse applications, such as catalysis,[10,11] sensing,[12,13] energy conversion,[14,15] and optics.[16] Amongst these, cuprous oxide (CuOH) has long been attracting extensive interest.[17,18] Back in the early 1900s, Miller and Gillett observed that when a NaCl solution was electrolyzed with copper working electrodes at low temperatures (below 60 °C), yellow CuOH precipitates were produced.[19,20] Subsequently, several studies were conducted to investigate the characteristic structure and properties of CuOH synthesized via various methods.[21–23] Nevertheless, in these early studies, CuOH was mostly in the bulk solid form and structurally metastable, where the yellowish precipitates would rapidly change the color appearance to dark red, signifying the formation of Cu_2O, upon exposure to the ambient or thermal treatment due to the lack of proper protection from oxidation and/or dehydration. Such structural instability makes it difficult to study the properties and applications of the obtained CuOH. In 2012, Korzhavyi et al.[24] carried out theoretical studies and demonstrated that CuOH could exist in a solid form; yet the metastability led to the formation of a random mixture of various configurations in the crystal structure, such as Cu_2O and ice VII H_2O. Soroka

Q. Liu, Y. Peng, D. DuBois, J. Tressel, F. Nichols, R. Mercado,
T. Assafa, D. Pan, G. Millhauser, S. Chen
Department of Chemistry and Biochemistry
University of California
1156 High Street, Santa Cruz, CA 95064, USA
E-mail: shaowei@ucsc.edu
Z. Masood, Q. Ge
School of Chemical and Biomolecular Sciences
Southern Illinois University
Carbondale, IL 62901, USA
E-mail: qge@chem.siu.edu

P. Ashby
Molecular Foundry
Lawrence Berkeley National Laboratory
Berkeley, CA 94720, USA
H.-L. Kuo, J. Q. Lu
School of Engineering
University of California
5200 North Lake Road, Merced, CA 95343, USA
F. Bridges
Department of Physics
University of California
1156 High Street, Santa Cruz, CA 95064, USA

**ADVANCED
SCIENCE NEWS**

www.advancedsciencenews.com

**ADVANCED
MATERIALS**

www.advmat.de

et al.[25] found that solid-state CuOH could indeed be produced, most likely in the hydrated form of CuOH × H$_2$O as an intermediate product of Cu$_2$O. In a combined theoretical and experimental study,[26] Korzhavyï's group showed that the ground-state structure of CuOH(s) consisted of both 1D polymeric (CuOH)$_n$ chains and 2D trilayer units, suggesting the possibility of nanosheet production. In addition, density functional theory (DFT) calculations have shown that CuOH is a semiconductor with a wide bandgap of 3.03 eV (or 2.73 eV in a cation-disorder form), suggestive of its potential optical/photocatalytic applications. However, it should be recognized that, to the best of our knowledge, thus far there has been no success in the experimental preparation of stable CuOH nanostructures.
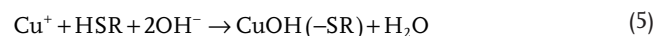
Organic ligands have been widely used in the surface functionalization and stabilization of metals and metal oxides,[27,28] hydroxides,[29] and chalcogenides.[30,31] For their nanoparticles, select organic ligands can be exploited for the manipulation of the shape,[32,33] size distribution,[34–36] and crystalline facets.[37] Significantly, with the protection of such an organic shell, not only the structural stability can be markedly enhanced,[38] new optical, electronic, and catalytic properties may also emerge, due to the unique interfacial interactions.[28,39,40] Thus, one immediate question arises: Can stable CuOH nanostructures be obtained by deliberate functionalization with select organic ligands? This is the primary motivation of the present study, where we demonstrate an effective strategy to synthesize stable CuOH nanostructures by surface functionalization with acetylene and mercapto derivatives.[28,39,40]

Specifically, for the first time ever, stable CuOH nanostructures were prepared by a facile wet-chemistry method. Experimentally, sulfite ions (SO$_3^{2-}$) were exploited as the reducing agent and added into a Cu^{2+} solution in a mixture of organic solvents in the presence of select acetylene and mercapto derivatives, with 4-ethylphenyacetylene (EPA), 1-hexadecyne (HC16) and 4-ethylphenylthiol (EPT) as the illustrating examples. The two acetylene derivatives were chosen, as prior studies have shown that alkyne ligands may impart unique electrical and optical properties to metal/metal oxide nanoparticles owing to the conjugated interfacial linkage that leads to intraparticle charge delocalization, which varies with the specific molecular structure of the aliphatic fragments, in contrast to mercapto derivatives like EPT that were involved in non-conjugated interfacial interactions.[28,39,41] Notably, acetylene derivatives have been known to bind to Cu^I centers forming polymeric nanostructures,[42,43] which may be conducive to the stabilization of the CuOH units. It was found that the resulting organically capped CuOH nanostructures were readily dispersible in organic media, and stable in both solution and solid forms. Microscopic and spectroscopic studies showed that the obtained CuOH nanostructures exhibited a nanoribbon morphology and were functionalized with Cu−C≡ and Cu−S− interfacial linkages, and the photoluminescence properties varied with the surface capping ligands due to a discrepancy of the charge transfer at the ligand-CuOH interface and hence the material bandgap. Consistent results were obtained in first principles calculations. Notably, the EPA-capped CuOH nanostructures manifested drastically enhanced photodynamic antibacterial activity, owing to the conjugated CuOH-EPA linkages that facilitated interfacial charge transfer and generation of reactive oxygen species (ROS) under UV and blue-light photoirradiation, in comparison to the EPT-capped counterparts.

2. Results and Discussion

Note that the direct mixing of Cu$^+$ and OH$^-$ led to the uncontrollable formation of yellow CuOH precipitates, which decayed rapidly within a day (Figure S1, Supporting Information). Thus, to prepare stable CuOH nanostructures, a unique synthetic procedure was developed in the present study by using Cu^{2+} and SO$_3^{2-}$ as the precursors. Briefly, a mixture of HSO$_3^-$ and OH$^-$ was injected into a Cu^{2+} solution in a mixed solvent of dichloromethane (DCM), N,N-dimethylformamide (DMF), and ethanol at the volumetric ratio of 1:1:1 in the presence of select organic capping ligands, producing a yellow solution that is consistent with CuOH (Figure S2, Supporting Information).[21–23] The experimental details are included in the Supporting information. The mixture of solvents was deliberately chosen to optimize the polarity of the solvents for good dispersion of both the copper salts and organic ligands. The production of organically capped CuOH nanostructures most likely involved the following reactions,

$$HSO_3^- + OH^- \rightleftharpoons SO_3^{2-} + H_2O \tag{1}$$

$$2Cu^{2+} + SO_3^{2-} + 2OH^- \rightarrow 2Cu^+ + SO_4^{2-} + H_2O \tag{2}$$

$$Cu^+ + OH^- \rightarrow CuOH \tag{3}$$

$$Cu^+ + HC \equiv CR + 2OH^- \rightarrow CuOH(-C \equiv CR) + H_2O \tag{4}$$

$$Cu^+ + HSR + 2OH^- \rightarrow CuOH(-SR) + H_2O \tag{5}$$

First, bisulfite ions were neutralized into sulfite upon the addition of KOH (equation 1), which then reduced Cu^{2+} into Cu$^+$, as the formal potential of the SO$_4^{2-}$/SO$_3^{2-}$ couple (E° = −0.936 V) is far more negative than that of Cu^{2+}/Cu$^+$ (+0.159 V) (equation 2).[44] The resulting Cu$^+$ subsequently reacted with OH$^-$ to produce cuprous hydroxide (CuOH) (equation 3); and in the presence of select organic ligands, such as acetylene (HC≡CR) and mercapto (HSR) derivatives, stable CuOH nanostructures were produced, due to the formation of CuOH−C≡C− and CuOH−S− interfacial bonds (equations 4 and 5),[45] as manifested by the apparent color change from blue to bright yellow (Figure S2, Supporting Information). Three samples were prepared using EPA, HC16, and EPT as the protecting ligands, and denoted as CuOH-EPA, CuOH-HC16, and CuOH-EPT, respectively. Note that in the synthesis of CuOH-EPT, the solution turned yellow upon the addition of EPT into Cu^{2+} before the addition of sulfite, likely due to the reduction of Cu^{2+} to Cu$^+$ by the thiol moieties.[46] Remarkably, all final products (CuOH) can be readily dispersed, and remain stable, in a range of organic media, such as DCM, tetrahydrofuran (THF), toluene, etc., suggesting sufficient protection by the hydrophobic organic ligands.[39] By contrast, without the addition of any organic ligands, greenish-yellow precipitates (CuOH) were formed at the bottom of the flask (Figure S3, Supporting Information); and X-ray photoelectron

spectroscopy (XPS) measurements showed the formation of CuO, which likely arose from the facile decomposition of CuOH upon exposure to the ambient, suggesting that the organic ligands played a critical role in stabilizing the formation of CuOH (Figure S1, Supporting Information). In another control experiment without the addition of the sulfite ions, only brownish precipitates were produced (Figure S4, Supporting Information), which was identified as CuO by XPS measurements, indicative of the critical role of sulfite ions in the reduction of Cu^{2+} into Cu^+ (equation 2). The solution pH was also important in the formation of stable CuOH. When the solution became too acidic (Figures S5 and S6, Supporting Information) or too alkaline (Figure S7, Supporting Information), other Cu compounds, such as CuO, Cu_2O, or cupric sulfates, would be produced instead. That is, a mildly alkaline condition is conducive to the stabilization of the ligand-capped CuOH nanostructures (Figure S8, Supporting Information). In fact, the obtained CuOH samples could be gradually decomposed in strong acid (2 M H_2SO_4) to a colorless solution (Figure S8, Supporting Information), consistent with the Cu^+ valence state and the formation of a hydroxide compound. In sharp contrast, the structural stability of the CuOH samples was significantly enhanced in neutral and mildly alkaline conditions, where the oxidation into Cu^{2+} was markedly impeded, in comparison to bare CuOH (Figures S1 and S3, Supporting Information), as manifested in XPS measurements (Figures S9–S12, Supporting Information).

The morphologies of the CuOH samples were first examined by transmission electron microscopic (TEM) measurements. One can see from **Figure 1**a that CuOH-EPA manifests a nanoribbon-like shape with a width in the range of 130 to 200 nm and a micron-scale length. The CuOH-HC16 (Figure 1b) and CuOH-EPT (Figure 1c) samples also exhibit a flaky structure but bundled into an irregular shape. High-resolution TEM measurements (Figure 1d–i) show that the samples actually

consisted of ultra-small nanoclusters of less than 2 nm in diameter with well-defined lattice fringes embedded within a largely amorphous scaffold, where the interplanar spacing was estimated to be ≈0.21 and 0.26 nm for both CuOH-EPA (Figure 1g) and CuOH-HC16 (Figure 1h) and 0.25 nm for CuOH-EPT (Figure 1i), corresponding to the (220), (210) and (0$\overline{2}$2) facets of CuOH, respectively.[26] Note that with an increasing initial feed of Cu^{2+}, larger CuOH nanoparticles were produced (dia. 5–10 nm, Figure S13, Supporting Information).

Consistent results were obtained in atomic force microscopy (AFM) measurements. From the topographic images in Figure 1j and Figures S14–S16 (Supporting Information), the three CuOH samples can all be seen to exhibit a 1D nanowire-like morphology. Line scans across the nanowire actually revealed a nanoribbon structure with a width of ≈200 nm and a thickness of ≈45 nm (Figure 1k), in good agreement with results from TEM measurements (Figure 1a–c).

The nanoribbon structures can also be resolved in scanning electron microscopy (SEM) measurements, where CuOH-EPA can be seen to contain nanoribbons of 5 to 7 μm in length (Figure S17, Supporting Information), whereas CuOH-HC16 (Figure S18, Supporting Information) and CuOH-EPT (Figure S19, Supporting Information) exhibit a mostly irregular flaky structure. Meanwhile, elemental mapping analysis based on energy dispersive X-ray (EDS) spectroscopy showed that all three CuOH samples featured a homogeneous distribution of Cu, O, and C, with S found also in CuOH-EPT, consistent with the formation of the respective ligand-capped nanoparticles. TEM-based EDS scans in higher magnifications showed consistent results (Figures S20–S22, Supporting Information).

Further structural insights were obtained in X-ray diffraction (XRD) measurements. Figure 1l depicts the XRD patterns of CuOH-EPA, which consists of only two sharp diffraction peaks at 2θ = 10.18° and 15.34°, corresponding to a d value of 0.87
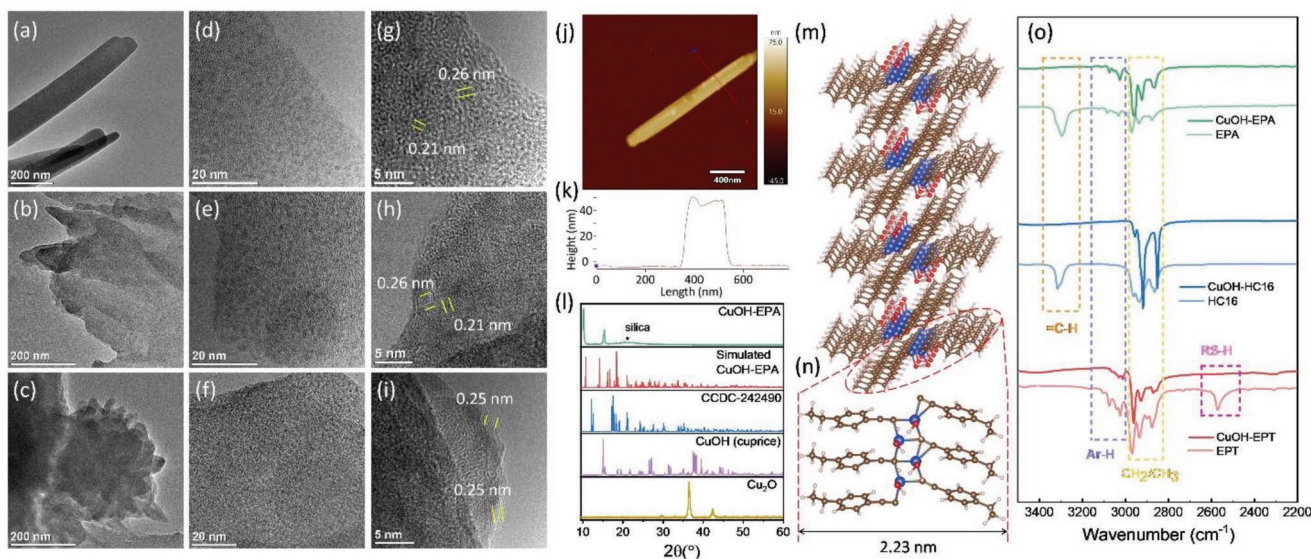

Figure 1. Representative TEM images of the organically capped CuOH samples: a,d,g) CuOH-EPA, b,e,h) CuOH-HC16, c,f,i) CuOH-EPT. Scale bars are a–c) 200 nm, d–f) 20 nm, and g–i) 5 nm. j) AFM topograph of CuOH-EPA and k) the corresponding height profile along the red line in panel (j). l) XRD patterns of CuOH-EPA, simulated CuOH-EPA, traditional Cu-alkyne polymer (CCDC-242490), CuOH (cuprice), and Cu_2O. m,n) Simulated CuOH-EPA structure. o) FTIR spectra of CuOH-EPA, CuOH-HC16, and CuOH-EPT nanostructures, and the corresponding ligand monomers (light-colored curves).

and 0.58 nm, respectively. Note that such patterns are markedly different from those of "cuprice" CuOH,[26] Cu_2O (RRUFF ID: R050374.1), and Cu^I-alkyne coordination polymers reported previously (CCDC-24290, Figure S23, Supporting Information).[42,43] Yet, the results are in excellent agreement with a layered structure where each layer consists of a 1D assembly of the CuOH-EPA moieties that is facilitated by hydrogen bonding interactions between the OH groups and π-π stacking between the phenyl rings of the EPA ligands (Figure 1m,n). In fact, the simulated XRD patterns exhibit two peaks at 2θ = 10.69° and 14.16° (the CIF files are included in the Supporting Information), very close to those of the CuOH-EPA sample.

Taken together, results from these characterizations suggest that the obtained samples consist of CuOH nanoclusters embedded within a CuOH-ligand nanoribbon nanostructure. Such a structure calls for a 1:1 molar ratio between CuOH and the organic ligands, which was indeed observed in XPS measurements (vide infra). Notably, the expected metal contents were also in excellent agreement with results from inductively coupled plasma-optical emission spectrometry (ICP-OES) measurements (Table S1, Supporting Information).

The surface structure of the obtained CuOH nanostructures was then characterized by Fourier transform infrared (FTIR) spectroscopic measurements. From Figure 1o, one can see that all three CuOH samples exhibited a broad peak ≈3400 cm^{-1} (Figure S24, Supporting Information), due to the O-H stretch.[25] In addition, in comparison to the spectra of the monomeric ligands, the organically capped CuOH samples all exhibited vibrational peaks in the range of 2800 to 3000 cm^{-1}, as highlighted by the yellow box, due to the CH_2/CH_3 stretches of the organic ligands. For both the CuOH-EPA and CuOH-EPT, additional vibrational features can be seen in the range of 3000 to 3100 cm^{-1} (purple box), due to the aromatic C-H stretches of the aryl ligands. Consistent profiles can be found in the fingerprint region of 810 to 830 cm^{-1} (Figure S25, Supporting Information). Meanwhile, as highlighted in the orange box, unlike their corresponding monomers, the terminal $\equiv$C-H vibration at 3293 - 3313 cm^{-1} vanished with CuOH-EPA and CuOH-HC16, indicating effective cleavage of the $\equiv$C—H bond and their anchorage onto the surface of CuOH, as observed previously.[28,39,40] A similar behavior can be seen with the CuOH-EPT sample, where the S-H vibration was well-defined at 2568 cm^{-1} for the EPT monomers, but disappeared altogether in CuOH-EPT (magenta box). Since no S-O vibration could be identified at 950–800 or 550 cm^{-1},[47] the EPT ligands were most likely bound onto the CuOH surface via the Cu-S-interfacial bonds, rather than Cu-O-S-. Notably, consistent results were obtained from DFT calculations (Table S2, Supporting Information). Of particular notice is the contributions of the OH moiety to the vibrational bands at ≈821.7, 1119, and 3583.1 cm^{-1} (Movie S1, Supporting Information), further confirming the formation of CuOH-EPA nanostructures. In addition, the peak at 547 cm^{-1} is most likely due to the Cu-C$\equiv$ vibration, suggesting that the alkyne ligands are bound to the Cu atomic site in CuOH (Figure 1m,n).

The interfacial bonding structure is further supported in Raman measurements. From Figure S26 (Supporting Information), both CuOH-EPA and CuOH-HC16 can be seen to exhibit multiple peaks in the range of 100 to 500 cm^{-1}, which can be

attributed to Cu-C$\equiv$ and Cu-OH vibrations. For instance, in CuOH-EPA the peaks at 120, 365, and 442 cm^{-1} may be attributed to the Cu-OH vibrations, and those at 174, 196, and 287 cm^{-1} due to the Cu-C$\equiv$ vibrations,[48] which further confirms that the EPA ligands are indeed directly bonded to Cu instead of O. In fact, these assignments are consistent with results from DFT calculations (Table S3, Movies S2 and S3, Supporting Information). For CuOH-HC16, the Cu-OH vibrations can be found at 125, 357, and 446 cm^{-1}, with the rest of the peaks arising from Cu-C$\equiv$ and C-C vibrations.[48] Meanwhile, the C$\equiv$C vibration can be readily resolved in both CuOH-EPA (493 cm^{-1}) and CuOH-HC16 (497 cm^{-1}), but absent in CuOH-EPT. In contrast, CuOH-EPT showed an intense peak at 110 cm^{-1} due to Cu-S vibrations.[49] In addition, no S-S vibrations can be identified at ≈470 cm^{-1} for CuOH-EPT, ruling out the formation of crystalline copper sulfides.[49]

XPS measurements were then carried out to analyze the elemental compositions and valance states of the samples (Figure S27, Supporting Information). **Figure 2**a depicts the high-resolution scans of the Cu 2p electrons, where the Cu $2p_{3/2}/2p_{1/2}$ peaks of all samples can be found at 932.0/951.8 eV for CuOH-EPA, 932.2/952.0 eV for CuOH-EPT, and 932.3/952.0 eV for CuOH-HC16. Note that no apparent satellite peaks that are characteristic of Cu^{2+} can be discerned from the Cu 2p spectra, indicating that Cu^{2+} was indeed effectively reduced by SO_3^{2-} to Cu^+ (equation 2).[50,51] This is in sharp contrast to the control experiments where samples were prepared in the same manner but without the addition of $NaHSO_3$ (Figure S4, Supporting Information). In fact, electron paramagnetic resonance (EPR) measurements (Figure 2b) show that all CuOH samples displayed only a featureless profile within the magnetic field strength of 2500 to 3500 G, in sharp contrast to $CuCl_2$ that exhibits a clearly-defined signal with a g value of 2.188. This is consistent with the diamagnetic nature of Cu^+ and paramagnetic Cu^{2+}.[51] The corresponding high-resolution XPS spectra of the O 1s electrons were exhibited in Figure 2c. One can see that a single component was resolved in all three CuOH samples, 530.5 eV for CuOH-EPA, 531.2 eV CuOH-HC16, and 531.4 eV for CuOH-EPT, that can be ascribed to metal hydroxide.[52] Notably, the red shift of 0.9 eV with CuOH-EPA and 0.2 eV with CuOH-HC16, as compared to CuOH-EPT, likely arose from the different charge transfer from CuOH to the ligands (vide infra). The results are also consistent with the variation of the valence band maximum (VBM) of the three samples. From the VBM spectra in Figure 2f, CuOH-EPA can be seen to possess the lowest VBM at 0.99 eV, in comparison to 1.31 eV for CuOH-HC16 and 1.61 eV for CuOH-EPT.

As for CuOH-EPT, the S 2p spectrum shows a well-defined doublet at 162.0/163.3 eV, which can be assigned to the $2p_{3/2}/2p_{1/2}$ electrons of Cu-S,[53,54] consistent with the stabilization of CuOH by Cu—S— interfacial bonds (Figure 2d). Notably, this species was totally absent in both CuOH-HC16 and CuOH-EPA, indicating that these samples were free of metal sulfide impurities.

The C 1s spectra of the three CuOH samples are depicted in Figure 2e, which are also consistent with their respective ligand structure.[41] For CuOH-EPA, deconvolution yields three peaks at 283.0 eV for sp-hybridized C, 283.8 eV for sp^2 C (aromatic rings), and 284.4 eV for sp^3 C. For CuOH-HC16, only the sp
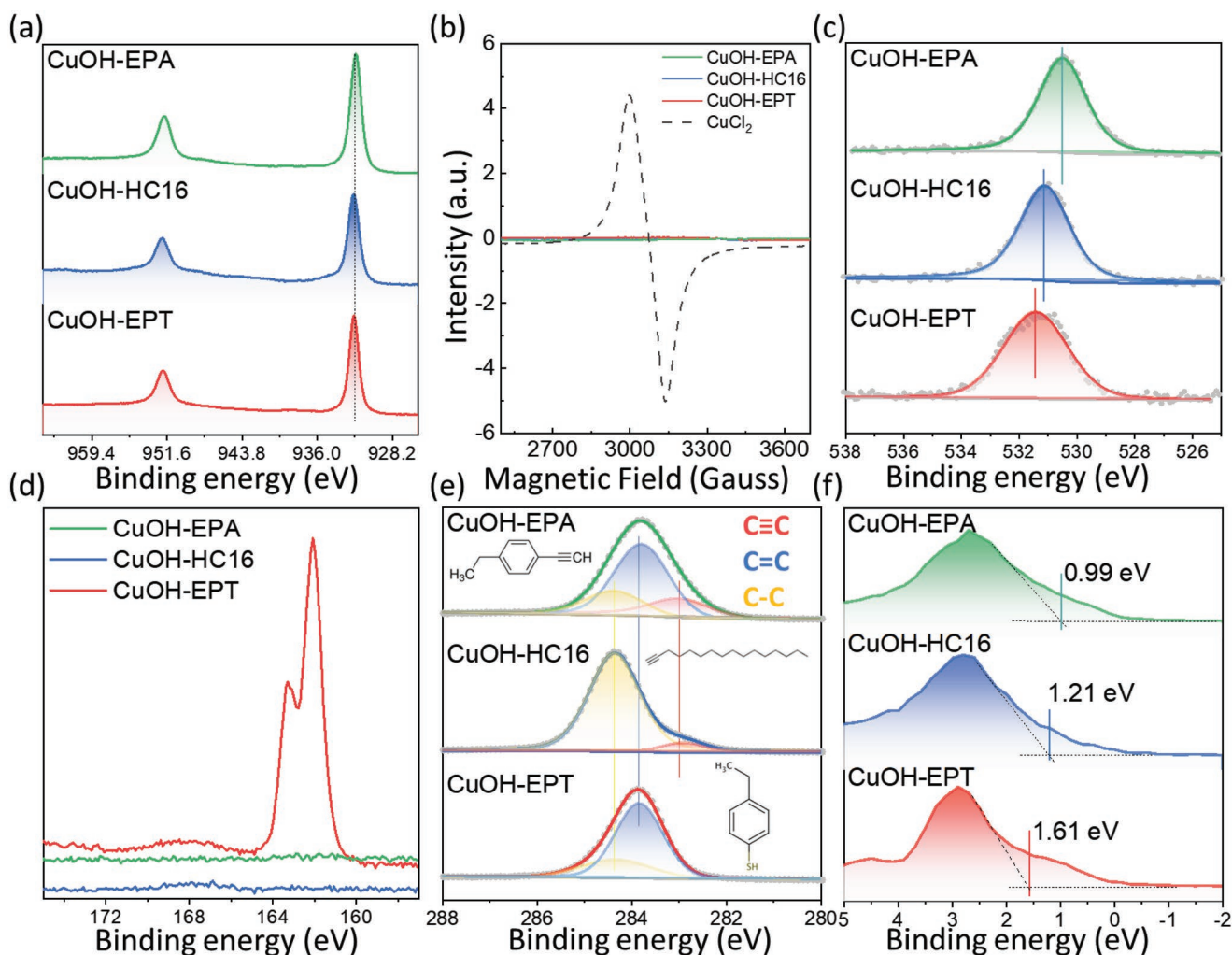
Figure 2. High-resolution XPS spectra of the a) Cu 2p, c) O 1s, d) S 2p, and e) C 1s electrons of the CuOH-EPA, CuOH-HC16, and CuOH-EPT samples (from top to bottom). The corresponding b) EPR and f) VBM spectra.

and sp^3 carbon can be resolved, and only the sp^2 and sp^3 species for CuOH-EPT. These results are also listed in Table S4 (Supporting Information), where the Cu:ligand molar ratio was indeed close to 1:1 for all samples, as suggested in the nanostructure shown in Figure 1m,n.

Notably, the XPS profiles of the three CuOH samples remained virtually invariant even after storage in ambient conditions for three months (Figure S28, Supporting Information), suggesting remarkable structural stability of the materials that was most likely endowed by the organic functionalization. This is a drastic deviation from the metastable characteristics observed with bare CuOH (Figure S3, Supporting Information) or bulk CuOH (Figure S1, Supporting Information).[24,25]

Further structural insights of CuOH-EPA were obtained from X-ray absorption spectroscopic (XAS) measurements. From the X-ray absorption near edge spectra (XANES) in **Figure 3**a, one can see that all three organically capped CuOH samples possessed an oxidation state close to that of Cu$_2$O, with the absorption edges situated between those of the Cu foil and CuO references. In fact, from the first-order derivatives of XANES (inset to Figure 3a), it can be seen that the three CuOH

samples all exhibit an extremum (pre-edge peak) at 8980 eV, very close to that of Cu$_2$O, but apparently different from those of Cu foil (8978 eV) and CuO (8982 eV). Specifically, CuOH-EPA and CuOH-HC16 can be seen to exhibit a pre-edge peak at 8982 and 8981 eV, respectively, due to the 1s → 4p$_x$/p$_y$ transitions, and such transitions occurred at 8981 eV for bulk Cu$_2$O. By contrast, CuOH-EPT exhibited only a shoulder at 8981 eV, suggesting a different chemical environment due to the formation of Cu−S interfacial bonds (vs Cu−C≡ for CuOH-EPA and CuOH-HC16), whereas bulk CuO showed an even less sharp shoulder at 8984 eV, due to the 1s to 4p$_z$ transition.[55] From the Fourier-transform extended X-ray absorption fine spectra (FT-EXAFS) in Figure 3b, one can see that the first main peak, which arose from the Cu-O/C path, appeared at 1.72 Å for CuOH-EPA, and increased to 1.82 Å for CuOH-HC16 and CuOH-EPT. These are all larger than those of bulk CuO (1.57 Å) and bulk Cu$_2$O (1.47 Å). Fitting of the EXAFS data (Figures S29–S31 and Table S5–S7, Supporting Information) shows that the bond length of Cu-O/C was rather consistent for CuOH-EPA and CuOH-HC16 at ≈2.01 and 2.05 Å, respectively, yet longer than those of the control samples of Cu$_2$O (1.85 Å)
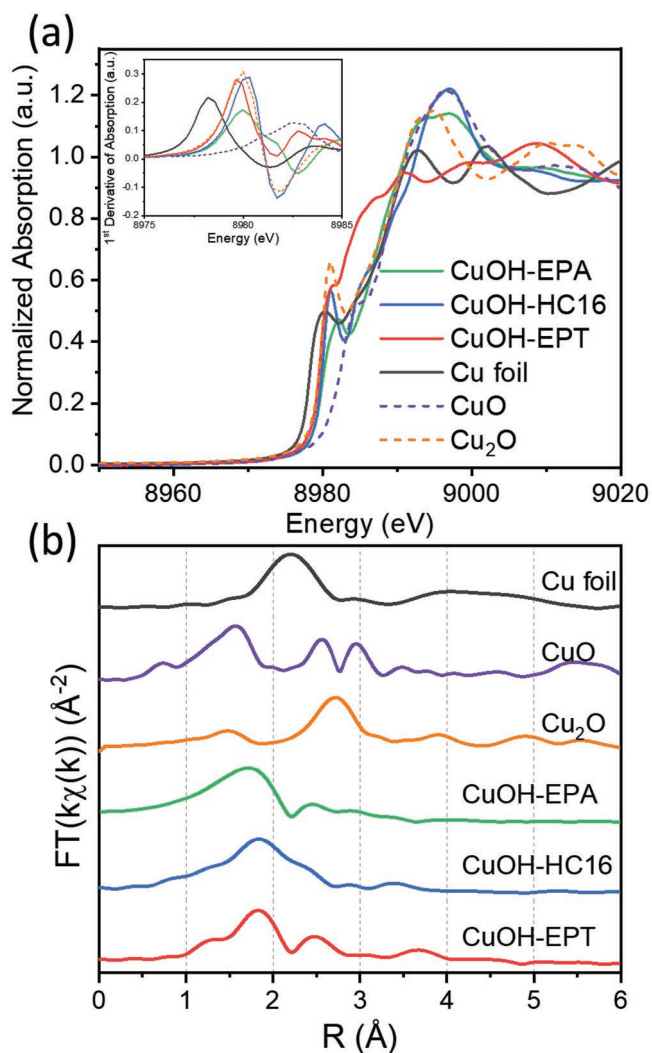
ADVANCED
SCIENCE NEWS
www.advancedsciencenews.com

ADVANCED
MATERIALS
www.advmat.de

Figure 3. a) Cu K-edge normalized XANES profiles of CuOH-EPA, CuOH-HC16, CuOH-EPT, Cu foil, Cu_2O, and CuO, and b) their corresponding FT-EXAFS spectra. Inset to panel (a) is the corresponding first-order derivative of the pre-edge region.

and CuO (1.95 Å), indicating the absence of copper oxides in the obtained sample. Additionally, the Cu-O/C coordination numbers (5.3 for CuOH-EPA and 5.8 for CuOH-HC16) were larger than that of Cu_2O (2) but consistent with the nanoribbon structure shown in Figure 1m,n,[56,57] suggestive of an imperfect layered structure of the CuOH-EPA and CuOH-HC16 samples. The second main peak at 2.4 Å of CuOH-EPA and CuOH-HC16 most likely arose from the second shell interaction of Cu−C with the organic capping ligands. By contrast, the first main peak of CuOH-EPT arose from the combined contributions of Cu−O/C and Cu−S bonds (Figure S31 and Table S7, Supporting Information), indicating the successful formation of the CuOH nanostructures capped by the EPT ligands, which is significantly different from CuOH-EPA and CuOH-HC16. Taken together, these results confirm the successful production of a Cu-O/C environment around Cu with no observable Cu-Cu interactions, suggesting an amorphous structure with little to no long-range crystallinity (vide ante).

To understand the interfacial structure and properties of the organically capped CuOH nanostructures, theoretical studies were performed by using the structural models proposed above (Figure 1m,n, and Figures S32 and S33, Supporting Information) anchored with EPA, butyne (HC4, as a simplified representation of HC16), and EPT. **Figure 4**a depicts the stable configuration of CuOH-EPA after relaxing, from which one can see that the acetylene moiety formed a Cu−C≡C− interfacial structure, which is consistent with the results from FTIR, Raman, and XPS measurements (Figure 1,2, and Figure S26, Supporting Information). Furthermore, one can see that the C≡C bond length increased slightly from 1.21 Å for the EPA monomer to 1.26 Å for CuOH-EPA (Figure 4a). These observations suggest effective electronic coupling at the CuOH-ligand interface, leading to the elongation of the acetylene moiety.[28] In fact, from the Bader charge profile in Figure 4a, one can see a charge transfer of ≈0.14 |e|, relative to the pristine EPA monomer, from CuOH to the EPA ligands. Charge accumulation in the −C≡C− interfacial bond and phenyl rings in CuOH-EPA are clearly visible in the charge density isosurfaces shown in Figure 4b. CuOH-HC4 shows a similar elongation and charge accumulation of the −C≡C− bond, where ≈0.38 |e| was transferred from CuOH to primarily −C≡C− (Figure 4c,d). Notably, the contribution of the ethyl group to interfacial charge transfer is minimal. This observation is consistent with the results of our prior study of alkyne-functionalized iridium nanoparticles and alkyne-functionalized TiO_2 nanoparticles.[28,58] In contrast, when EPT ligands were bound onto the CuOH cores, the interfacial linkage actually consisted of non-conjugated Cu−S− bonds (Figure 4e,f). In this case, there are obvious charge depletions in the S−H and S−Cu interfacial bonds and accumulations in the S-C bond, with a net charge transfer from CuOH to the ligand being 1.38 |e|. Considering that the Cu atoms exhibit a similar valence state from the afore-mentioned XPS, XAS, and charge analysis, the depletion of electrons in Cu-OH units will render a positive shift of the O 1s binding energies, which is in excellent agreement with results from XPS measurements (Figure 2c).

Notably, such different interfacial linkages resulted in a marked variation in the optical and electronic properties of the CuOH nanostructures. As mentioned earlier, the samples can all be readily dispersed in typical organic solvents (e.g., DCM, THF, etc) and remain stable without obvious precipitation. The photographs of the suspensions are shown in **Figure 5**a, where the color was grey-yellow for CuOH-EPT, and dark-yellow for CuOH-EPA and CuOH-HC16. Under photoirradiation with a UV lamp (≈365 nm), the samples can be seen to emit orange-red, yellow, and orange photons for the CuOH-EPT, CuOH-EPA, and CuOH-HC16 samples, respectively (Figure 5b). Notably, the color appearance of the DCM solutions was the same as that when they were dropcast onto a glass slide forming a solid film (Figure 5c). These observations indicated that the optical (and hence electronic) properties are different when CuOH was passivated by different organic ligands, as manifested in UV–vis and photoluminescence (PL) spectroscopic measurements (Figure 5d–i). One can see that CuOH-EPT exhibited an exponential decay profile in UV–vis measurements, without any apparent absorption features (Figure 5h),[59] whereas two main peaks can be resolved at 492 and 406 nm for CuOH-EPA (Figure 5d), and one peak at 424 nm for CuOH-HC16
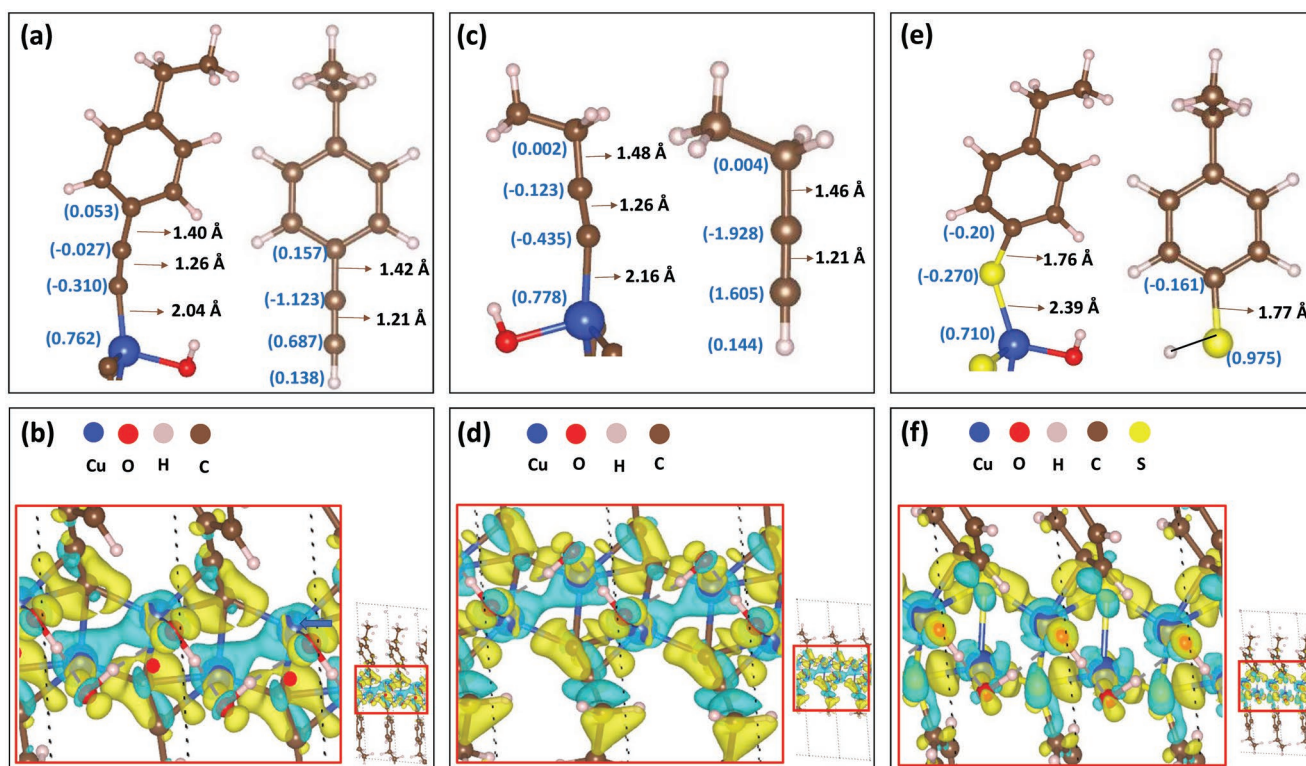
Figure 4. Optimized structure of a) CuOH-EPA and EPA ligand, c) CuOH-HC4 and HC4, e) CuOH-EPT and EPT with corresponding bond distances (black) and Bader charges in |e| (blue). Charge density difference isosurfaces of b) CuOH-EPA, d) CuOH-HC4, and f) CuOH-EPT (±0.0016|e|). Yellow, positive representing electron gains; cyan, negative for electron loss.

(Figure 5f). At the same excitation wavelength (λ_{ex}) of 405 nm, both CuOH-EPT and CuOH-HC16 showed a PL emission peak (λ_{em}) at 650 nm (Figure 5d and 5f), whereas the emission peak of CuOH-EPA blue-shifted to 512 nm (Figure 5h). Interestingly, for this CuOH sample series, whereas λ_{em} remains virtually unchanged when λ_{ex} was varied within the range of 360 to 445 nm, the emission intensity diminished markedly at $\lambda_{ex} > 400$ nm for CuOH-EPT (Figure 5i) and at $\lambda_{ex} < 385$ nm for CuOH-HC16 (Figure 5g), but exhibited no clear diminishment with CuOH-EPA (Figure 5e).

To unravel the origins of the different optical properties amongst the samples, we calculated the density of states (DOS) of CuOH-EPA, CuOH-HC4, and CuOH-EPT. From Figure S34 (Supporting Information), one can clearly see that both CuOH-EPA and CuOH-HC4 exhibited a lower VBM position than CuOH-EPT, consistent with the experimental results shown in Figure 2f. To further discern the difference between CuOH-EPA and CuOH-HC4, projected local DOS (PDOS) were deconvoluted and shown in **Figure 6**a. It can be seen that whereas both structures showed extensive interfacial charge delocalization, the phenyl ring of EPA anchored on CuOH (CuOH-EPA) made a significant contribution to the states near the Fermi level (E_f) at the both VB and the conduction band (CB), in comparison to CuOH-HC4. A schematic illustration of PL emission is depicted in Figure 6b. For all samples, electrons are excited from the VB (contributed mainly by Cu−C≡C− interfacial bonds) to the CB (contributed mainly by the π electrons of the capping ligands) under appropriate photoexcitation. For

the HC_x (x = 16 for experimental and x = 4 for theory) capped CuOH nanostructures, the excitons relax to the CB edge and then return to the holes to emit light at ≈650 nm. The situation for CuOH-EPA is different. In the recombination process, the excitons relax to the dominating states from the phenyl ring rather than the CB edge before combining with the hole states in the ring. As a result, it emits light with higher energy (shorter wavelength at ≈512 nm).

This emission mechanism is supported by the calculated UV-vis spectra based on time-dependent DFT (TDDFT), as depicted in Figure 6c, where the four absorption peaks of CuOH-EPA observed experimentally in Figure 5d (314, 335, 406, and 492 nm) can be clearly identified (marked with asterisks). Figure 6d presents the natural transition orbitals (NTOs) for CuOH-EPA. NTOs are unitary transformations of the ordinary molecular orbitals to enable an intuitive qualitative description of electronic excitations. The NTOs are more compact and express the excitation as pairs of NTO orbitals, with transitions occurring from excited particles (OTOs) to the empty hole (UTOs). As shown in Figure 6d, the hole states are largely localized on the ligands, whereas the particle states concentrate on the CuOH units except for 314 nm. These characteristics are manifestations of strong interactions between the ligand and the CuOH core, which enable charge transfer excitation from the ligands to the particle and is likely the origin of the intense emissions across a wide range of excitation wavelengths, as shown in Figure 5e, indicating that the optical property of CuOH-EPA was dominated by the EPA ligands, consistent with
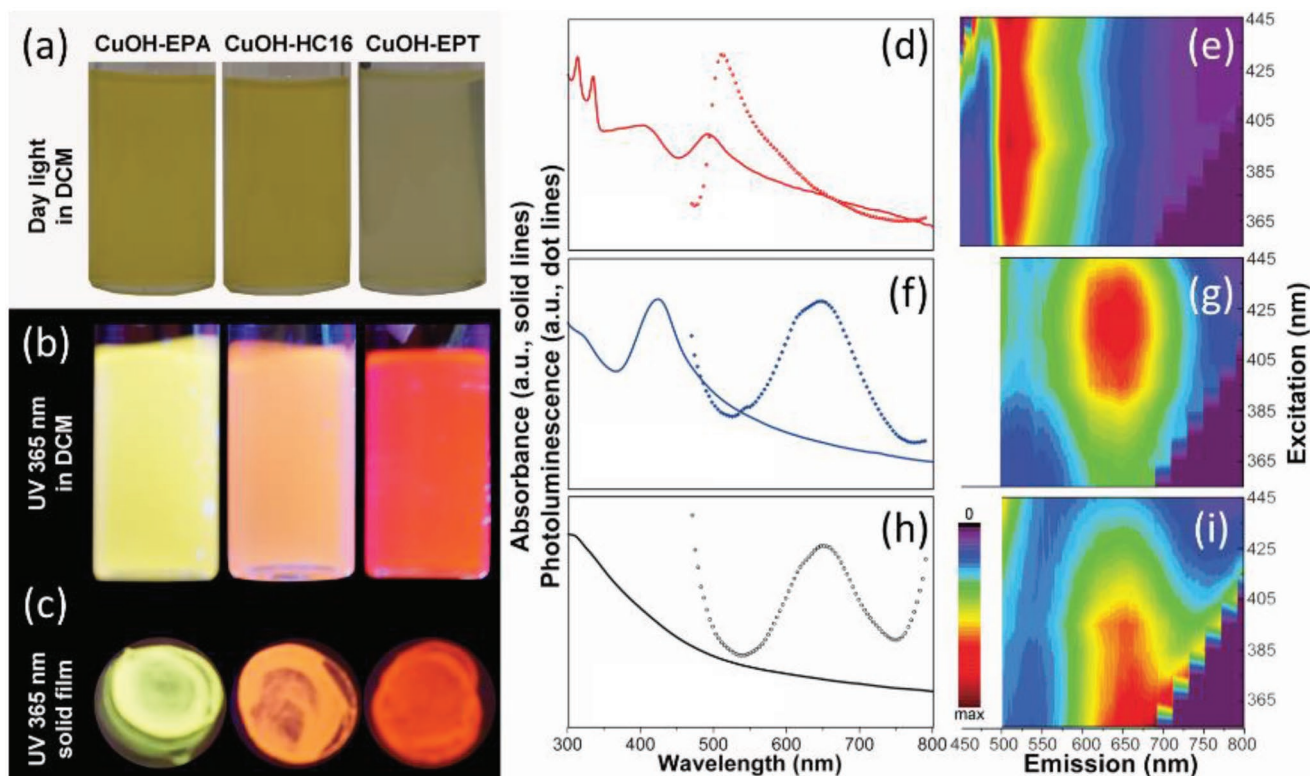
**ADVANCED
SCIENCE NEWS**

www.advancedsciencenews.com

**ADVANCED
MATERIALS**

www.advmat.de

Figure 5. Photographs of different organically capped CuOH nanostructures a) in ambient light (dispersed in DCM) and under 365 nm photoirradiation b) when dispersed in DCM and c) as solid films). The colors of the CuOH-EPA, CuOH-HC16, and CuOH-EPT dispersions in DCM are all yellowish, while the photoluminescence is red, yellow, and orange, respectively when dispersed in DCM or solid films. UV–vis (solid curves) and PL spectra (dotted curves) of d) CuOH-EPA, f) CuOH-HC16, and h) CuOH-EPT nanostructures at the excitation at 395 nm, and the excitation-dependent PL profiles of e) CuOH-EPA, g) CuOH-HC16, and i) CuOH-EPT.

the results from PDOS analysis. In contrast, for the CuOH-HC4 sample (Figure S35, Supporting Information), one can see that most OTOs and UTOs are localized on CuOH instead of the HC4 ligands, suggesting a diminished ligand-core interaction due to the lack of phenyl rings. Therefore, the emissions of CuOH-EPT and CuOH-HC16 are most likely dominated by the semiconducting CuOH cores.

With such unique optoelectronic properties, the ligand-capped CuOH nanostructures exhibited apparent photodynamic activity toward the inhibition of bacterial growth by using *Escherichia coli* (*E. coli*) as the illustrating example, and the antibacterial activity varied markedly among the sample series. Note that in the dark, none of the CuOH samples exhibited any antimicrobial activity (Figure S36, Supporting Information). Yet, under UV photoirradiation for up to 40 min (**Figure 7**a), the bacterial growth was significantly inhibited by CuOH-EPA and CuOH-EPT, where it took only 12 min to remove 50% of the bacterial cells with the former and 16 min for the latter, whereas virtually no inhibition was observed with CuOH-HC16, as compared to the *E. coli* control. The overall activity was diminished somewhat under blue light irradiation (465 nm). From Figure 7b, one can see that the growth of *E. coli* was significantly inhibited by CuOH-EPA only, with no survival of bacterial cells after two hours' exposure, and the antibacterial activity was minimal with CuOH-HC16 and CuOH-EPT. Taken together, these results indicate that CuOH-EPA stood out as the best antibacterial agent among the series.

Notably, no copper species were detected by ICP-OES measurements in the bacterial culture medium with CuOH-EPA (after 120 min), in comparison to 1.935 ppm with Cu_2O, signifying no leaching of Cu ions in the former. In Ellman's assay (Figure 7d), where the loss of GSH is an effective representation of oxidative stress,[60] it can be seen that under blue light irradiation for up to 2 h, CuOH-EPA led to the most significant degradation of GSH among the series, suggesting that the high antibacterial activity of CuOH-EPA was most likely due to the substantial oxidative stress produced under photoexcitation. This was indeed confirmed in EPR measurements. From Figure 7e, one can see that after blue light photoirradiation for 10 min, the CuOH-EPA and CuOH-HC16 samples manifested a clear 1:2:2:1 hyperfine structure within the magnetic field strength of 3275–3350 G, with a g value of 2.005 ($a_H = a_N = 14.9$ G), which is characteristic of the DMPO–OH adducts,[61] suggesting the formation of hydroxyl (HO•) radicals. By contrast, for CuOH-EPT and blank water, only a much weaker sextet hyperfine structure was observed within the same magnetic field range (g = 2.006, $a_N = 15.625$ G, and $a_H = 6.64$ G), which can be ascribed to the DMPO-OOH adduct stemming from superoxide radicals ($O_2^{\bullet-}$).[61,62] These observations are consistent with the significantly higher bactericidal activity of CuOH-EPA and CuOH-HC16, as compared to CuOH-EPT (Figure 7a,b), as hydroxyl radicals are far more active in antibacterial action than superoxide radicals.[63] Additionally, CuOH-EPA can be seen to exhibit the highest peak-to-peak intensity among the series, in excellent agreement with
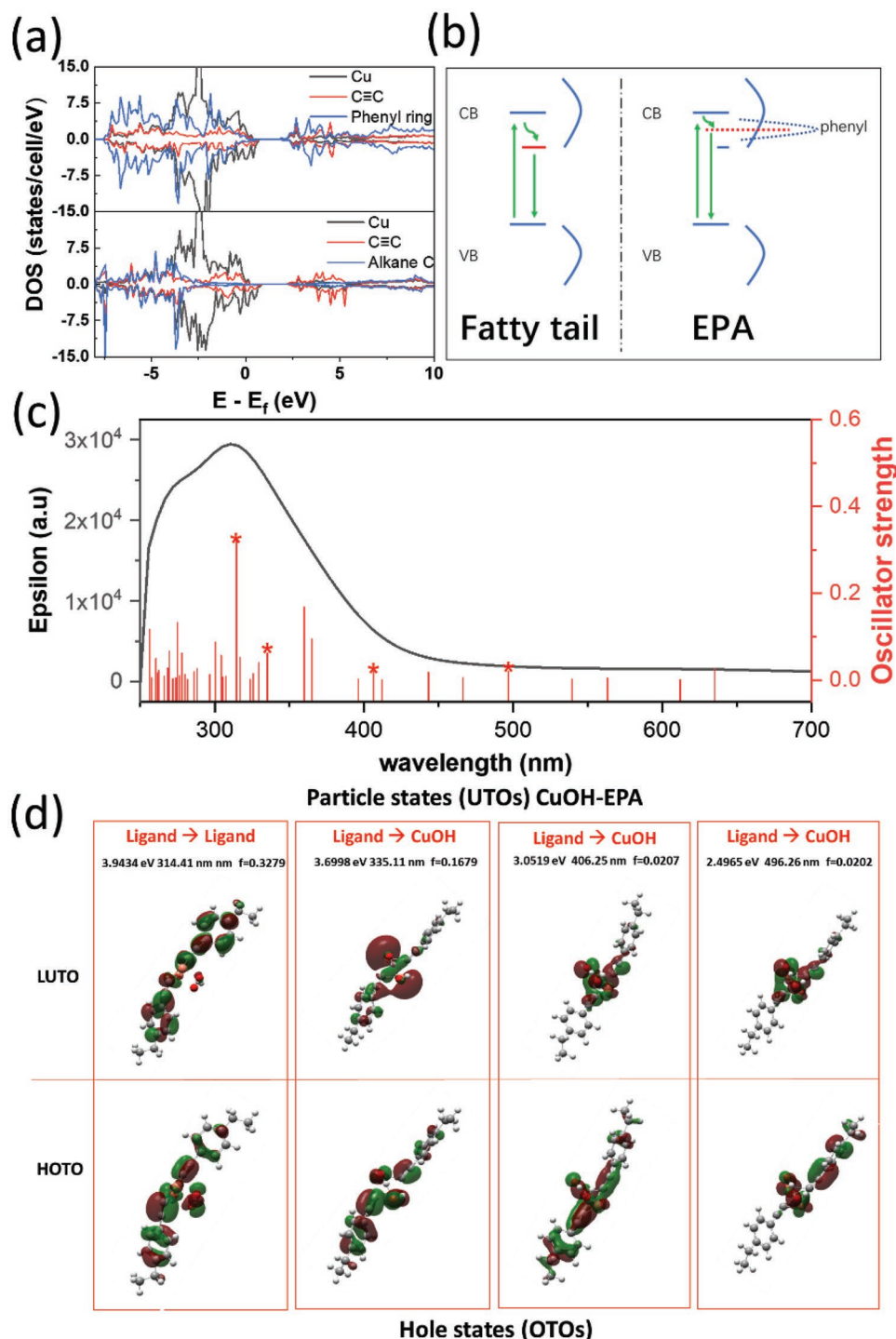
Figure 6. a) Projected local density of states of CuOH-EPA (top) and CuOH-HC4 (bottom). b) Proposed PL mechanism. c) TDDFT-based UV–vis spectrum of CuOH-EPA, where the asterisks denote experimental values. d) Natural transition orbitals (NTO) analysis of CuOH-EPA.

the greatest oxidative stress observed in Ellman's assay and the best antibacterial activity among the series.

In fact, the EPR signal intensity of CuOH-EPA exhibited a noticeable diminishment upon the addition of ethylenediaminetetraacetic acid (EDTA) and much less so with ascorbic acid (Figure S37, Supporting Information), which is the effective scavenger for photogenerated holes and superoxide radicals,

respectively.[61] This suggests that the HO• radicals were produced mainly by the hole oxidation of water, $H_2O + h^+ \rightarrow HO\bullet + H^+$, with a minor contribution from the disproportionation reaction of $O_2^{\bullet-}$.[63]

The markedly enhanced antibacterial activity of CuOH-EPA, as compared to others in the series, can be ascribed to its low bandgap (E_g) of 2.52 eV, as compared to CuOH-HC16 (2.94 eV)
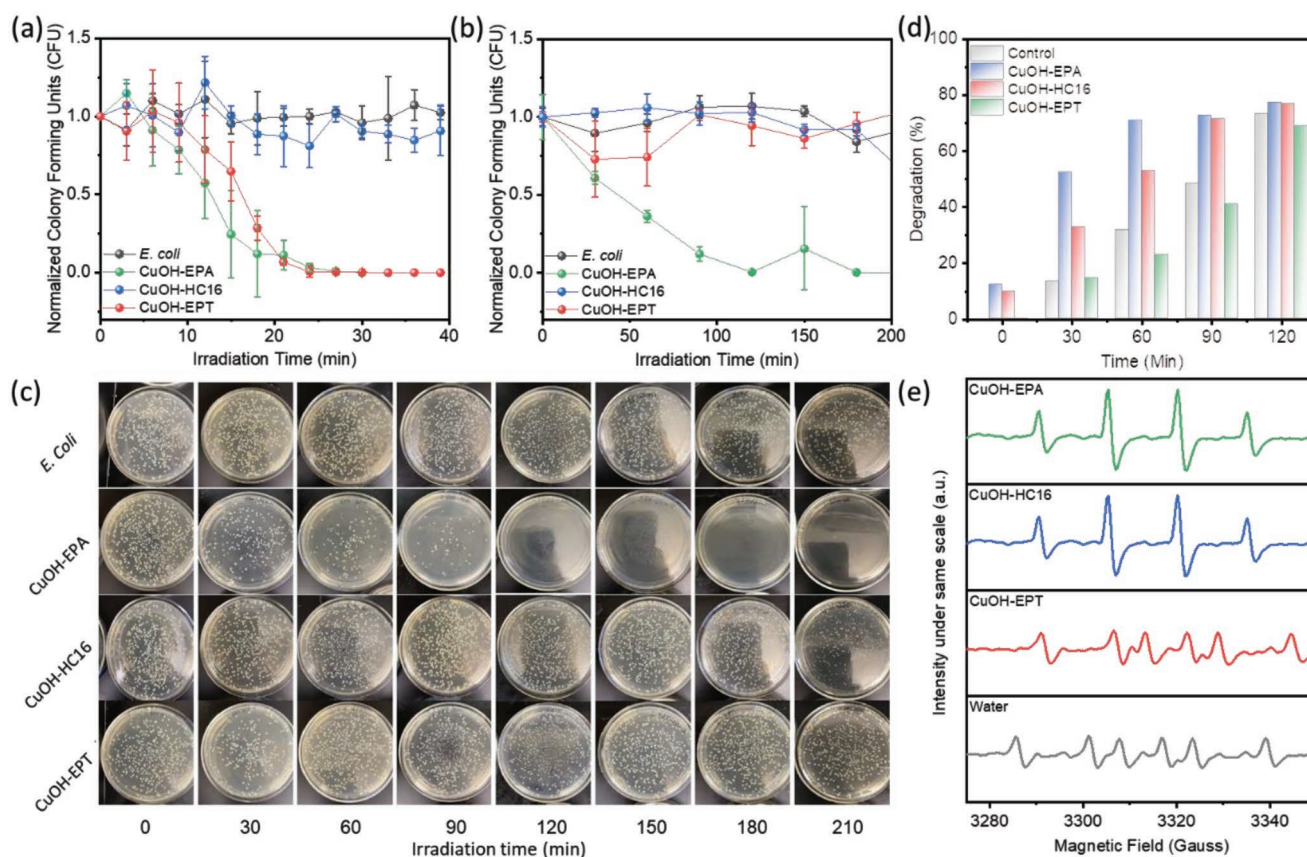
Figure 7. Antibacterial study of CuOH samples series. a) Study under UV photoirradiation for 40 min. Gram-negative bacteria E. coli is a control for comparison with CuOH containing samples. b) Study under blue Light (465 nm) for 200 min. Antibacterial studies under blue light photoirradiation. *E. coli* in PBS 1X (black line) is a control. Error bars are included as the study was done in triplicate. c) Photographs depicting *E. coli* grown on LB agar plates at different photoirradiation time points (i.e., 0, 30, 60, 90, 120, 150, 180, and 210 min) under blue light (465 nm) in the absence of CuOH and the presence of CuOH-EPA, CuOH-HC16, and CuOH-EPT. d) Loss of GSH after treatment by materials at different time points. e) EPR hyperfine splitting patterns in the presence of DMPO after 10 min of photoirradiation at 465 nm.

and CuOH-EPT (2.96 eV) (Figure S38, Supporting Information). This is consistent with results from DFT calculations (Figure S34, Supporting Information), CuOH-EPA (1.02 eV) < CuOH-EPT (1.46 eV) < CuOH-HC4 (1.64 eV) — note that DFT (PBE) typically underestimates the bandgap of solids.[64] Experimentally, the energy of the blue light photons (465 nm, 2.66 eV) is sufficiently high to excite the valence electrons of CuOH-EPA to the conduction band facilitating the generation of ROS and the eventual antimicrobial activity, but not high enough for CuOH-HC16 and CuOH-EPT.[60,65]

The discrepancy of interfacial charge transfer between the organic capping ligands and CuOH cores was further evidenced in cyclic voltammetry (CV) and electrochemical impedance measurements. From the CV profiles in Figure S39 (Supporting Information), both CuOH-EPA and CuOH-HC16 can be seen to exhibit an anodic peak at ≈+0.85 V, due to the oxidation of Cu$^+$ to Cu^{2+},[66,67] and the peak potential was substantially more positive at ≈+1.0 V with CuOH-EPT, consistent with the variation of the VBM observed in XPS measurements (Figure 2f). From the Mott–Schottky plots (Figure S40, Supporting Information), one can see that all CuOH samples exhibited a positive slope (m), suggestive of an n-type semiconductor.[68] The corresponding charge carrier densities (N_d) were then derived from the plots

by using $N_d = \dfrac{2}{e\varepsilon\varepsilon_0 m}$, with e being the elementary charge of an electron, ε the dielectric constant, and ε_0 the vacuum permittivity, which decreased markedly in the order of CuOH-EPA (7.54×10^4 cm^{-3}) > CuOH-HC16 (4.78×10^4 cm^{-3}) > CuOH-EPT (9.58×10^3 cm^{-3}). The markedly higher charge carrier density of CuOH-EPA and CuOH-HC16 can be ascribed to the conjugated CuOH-ligand interfacial linkages that facilitated intraparticle charge delocalization and hence interfacial charge transfer, a critical step in the photocatalytic generation of ROS, in comparison to the CuOH-EPT sample that involved nonconjugated interfacial bonds instead.[69,70]

3. Conclusions

In summary, for the first time ever, a facile wet-chemistry procedure was developed for the preparation of stable CuOH nanostructures in the presence of select organic ligands, such as acetylene and mercapto derivatives, where sulfite ions were exploited as the reducing agent. Electron microscopic study showed that the resulting CuOH nanostructures exhibited a nanoribbon morphology, and spectroscopic measurements

confirmed the anchoring of the acetylene moieties onto the CuOH surface forming Cu—C≡ interfacial linkage, whereas for the mercapto ligands, Cu—S— bonds. The former was found to lead to effective electronic coupling between the ligand π electrons and CuOH cores, in contrast to the latter which entailed mostly non-conjugated interfacial bonding interactions, as manifested in optical measurements and confirmed in theoretical studies based on DFT calculations. Significantly, with such unique optoelectronic properties, the CuOH-EPA stood out as the best antibacterial agent among the sample series under both UV and blue light irradiation, due to the effective production of hydroxyl radicals. This was largely ascribed to the hole oxidation of water that was facilitated by the conjugated core-ligand linkages and a narrowed bandgap. Results from this study suggest that functionalization by select organic ligands may be an effective strategy in the stabilization and functionalization of CuOH nanostructures, a key step toward their practical applications.

Supporting Information

Supporting Information is available from the Wiley Online Library or from the author.

Conflict of Interest

The authors declare no conflict of interest.

Data Availability Statement

The data that support the findings of this study are available from the corresponding author upon reasonable request.

[1] M. Yin, C.-K. Wu, Y. Lou, C. Burda, J. T. Koberstein, Y. Zhu, S. O'Brien, *J. Am. Chem. Soc.* **2005**, *127*, 9506.

[2] T. D. Golden, M. G. Shumsky, Y. Zhou, R. A. VanderWerf, R. A. VanLeeuwen, J. A. Switzer, *Chem. Mater.* **1996**, *8*, 2499.

[3] X. Wu, H. Bai, J. Zhang, F. Chen, G. Shi, *J. Phys. Chem. B* **2005**, *109*, 22836.

[4] X. S. Peng, J. Jin, I. Ichinose, *Adv. Funct. Mater.* **2007**, *17*, 1849.

[5] P. L. Saldanha, R. Brescia, M. Prato, H. Li, M. Povia, L. Manna, V. Lesnyak, *Chem. Mater.* **2014**, *26*, 1442.

[6] S. Wang, A. Riedinger, H. Li, C. Fu, H. Liu, L. Li, T. Liu, L. Tan, M. J. Barthel, G. Pugliese, F. De Donato, M. S. D'Abbusco, X. Meng, L. Manna, H. Meng, T. Pellegrino, *ACS Nano* **2015**, *9*, 1788.

[7] X. Zhao, G. Niu, J. Zhu, B. Yang, J.-H. Yuan, S. Li, W. Gao, Q. Hu, L. Yin, K.-H. Xue, E. Lifshitz, X. Miao, J. Tang, *J. Phys. Chem. Lett.* **2020**, *11*, 1873.

[8] R. Peng, M. Li, D. Li, *Coord. Chem. Rev.* **2010**, *254*, 1.

[9] M. Guan, Y. Jian, J. Sun, T. Shang, Q. Liu, Z. Xu, *CrystEngComm* **2015**, *17*, 7372.

[10] J. Singh, V. Kumar, K.-H. Kim, M. Rawat, *Environ. Res.* **2019**, *177*, 108569.

[11] L. Isac, C. Cazan, A. Enesca, L. Andronic, *Front. Chem.* **2019**, *7*, 694.

[12] P. Samarasekara, N. T. R. N. Kumara, N. U. S. Yapa, *J. Phys.: Condens. Matter* **2006**, *18*, 2417.

[13] S. Goel, F. Chen, W. Cai, *Small* **2014**, *10*, 631.

[14] J. Li, Y. Kuang, Y. Meng, X. Tian, W.-H. Hung, X. Zhang, A. Li, M. Xu, W. Zhou, C.-S. Ku, C.-Y. Chiang, G. Zhu, J. Guo, X. Sun, H. Dai, *J. Am. Chem. Soc.* **2020**, *142*, 7276.

[15] S. Nitopi, E. Bertheussen, S. B. Scott, X. Liu, A. K. Engstfeld, S. Horch, B. Seger, I. E. L. Stephens, K. Chan, C. Hahn, J. K. Norskov, T. F. Jaramillo, I. Chorkendorff, *Chem. Rev.* **2019**, *119*, 7610.

[16] M. Porta, M. T. Nguyen, T. Tokunaga, Y. Ishida, W.-R. Liu, T. Yonezawa, *Langmuir* **2016**, *32*, 12159.

[17] M. Tariq, M. D. Koch, J. W. Andrews, K. E. Knowles, *J. Phys. Chem. C* **2020**, *124*, 4810.

[18] K. Sekar, C. Chuaicham, U. Balijapalli, W. Li, K. Wilson, A. F. Lee, K. Sasaki, *Appl. Catal., B* **2021**, *284*, 119741.

[19] D. Miller, *J. Phys. Chem.* **1909**, *13*, 256.

[20] H. W. Gillett, *J. Phys. Chem.* **1909**, *13*, 332.

[21] K. L. Cheng, *Anal. Chem.* **1955**, *27*, 1165.

[22] T. P. Nevell, O. P. Singh, *Text. Res. J.* **1986**, *56*, 270.

[23] C. J. Whitham, H. Ozeki, S. Saito, *J. Chem. Phys.* **2000**, *112*, 641.

[24] P. A. Korzhavyi, I. L. Soroka, E. I. Isaev, C. Lilja, B. Johansson, *Proc. Natl. Acad. Sci. USA* **2012**, *109*, 686.

[25] I. L. Soroka, A. Shchukarev, M. Jonsson, N. V. Tarakina, P. A. Korzhavyi, *Dalton Trans.* **2013**, *42*, 9585.

[26] Y. G. Li, C. M. Lousada, I. L. Soroka, P. A. Korzhavyi, *Inorg. Chem.* **2015**, *54*, 8969.

[27] T. Rajh, L. X. Chen, K. Lukas, T. Liu, M. C. Thurnauer, D. M. Tiede, *J. Phys. Chem. B* **2002**, *106*, 10543.

[28] Y. Peng, B. Lu, F. Wu, F. Zhang, J. E. Lu, X. Kang, Y. Ping, S. Chen, *J. Am. Chem. Soc.* **2018**, *140*, 15290.

[29] W. Chen, H. Zuo, E. Zhang, L. Li, P. Henrich-Noack, H. Cooper, Y. Qian, Z. P. Xu, *ACS Appl. Mater. Interfaces* **2018**, *10*, 20326.

[30] M. P. Hendricks, M. P. Campos, G. T. Cleveland, I. Jen-La Plante, J. S. Owen, *Science* **2015**, *348*, 1226.

[31] M. V. Kovalenko, M. Scheele, D. V. Talapin, *Science* **2009**, *324*, 1417.

[32] Y. Sun, Y. Xia, *Science* **2002**, *298*, 2176.

[33] Y. Xia, Y. Xiong, B. Lim, S. E. Skrabalak, *Angew. Chem., Int. Ed.* **2009**, *48*, 60.

[34] V. P. Ananikov, N. V. Orlov, I. P. Beletskaya, V. N. Khrustalev, M. Y. Antipin, T. V. Timofeeva, *J. Am. Chem. Soc.* **2007**, *129*, 7252.

[35] Y. Xiong, I. Washio, J. Chen, H. Cai, Z.-Y. Li, Y. Xia, *Langmuir* **2006**, *22*, 8563.

[36] M. Dasog, G. B. De los Reyes, L. V. Titova, F. A. Hegmann, J. G. C. Veinot, *ACS Nano* **2014**, *8*, 9636.

[37] M.-H. Jao, C.-F. Lu, P.-Y. Tai, W.-F. Su, *Cryst Growth Des* **2017**, *17*, 5945.

[38] R. B. Grubbs, *Polym. Rev.* **2007**, *47*, 197.

[39] P. Hu, L. Chen, X. Kang, S. Chen, *Acc. Chem. Res.* **2016**, *49*, 2251.

[40] Y. Peng, Q. Liu, S. Chen, *Chem. Rec.* **2020**, *20*, 41.

[41] Y. Peng, J. E. Lu, C. P. Deming, L. Chen, N. Wang, E. Y. Hirata, S. Chen, *Electrochim. Acta* **2016**, *211*, 704.

[42] M. N. Uddin, M. S. Amin, M. S. Rahman, S. Khandaker, W. Shumi, M. A. Rahman, S. M. Rahman, *Appl. Organomet. Chem.* **2021**, *35*, e6067.

[43] Z. Wei, J. Hu, K. Zhu, W. Wei, X. Ma, Y. Zhu, *Appl. Catal., B* **2018**, *226*, 616.

[44] A. J. Bard, B. Parsons, J. Jordon, *Standard Potentials in Aqueous Solution*, M. Dekker, New York, **2017**.

[45] N. J. Long, C. K. Williams, *Angew. Chem., Int. Ed.* **2003**, *42*, 2586.

[46] S. Chen, A. C. Templeton, R. W. Murray, *Langmuir* **2000**, *16*, 3543.

[47] B. P. Vinayan, Z. Zhao-Karger, T. Diemant, V. S. K. Chakravadhanula, N. I. Schwarzburger, M. A. Cambaz, R. J. Behm, C. Kubel, M. Fichtner, *Nanoscale* **2016**, *8*, 3296.

[48] H.-Y. Jiang, P. Zhou, Y. Wang, R. Duan, C. Chen, W. Song, J. Zhao, *Adv. Mater.* **2016**, *28*, 9776.

[49] S. Wang, S. Jiao, J. Wang, H.-S. Chen, D. Tian, H. Lei, D.-N. Fang, *ACS Nano* **2017**, *11*, 469.

[50] C. Zhu, A. Osherov, M. J. Panzer, *Electrochim. Acta* **2013**, *111*, 771.

[51] T.-T. Sun, M. Wu, X.-W. He, W.-Y. Li, X.-Z. Feng, *J. Mater. Chem. B* **2015**, *3*, 6971.

[52] B. Jia, R. Hao, Z. Huang, P. Hu, L. Li, Y. Zhang, L. Guo, *J. Mater. Chem. A* **2019**, *7*, 4383.

[53] Y. Huai, Y. Qian, Y. Peng, *Appl. Surf. Sci.* **2020**, *531*, 147334.

[54] N. Wang, L. Li, D. Zhao, X. Kang, Z. Tang, S. Chen, *Small* **2017**, *13*, 1701025.

[55] J.-D. Yi, R. Xie, Z.-L. Xie, G.-L. Chai, T.-F. Liu, R.-P. Chen, Y.-B. Huang, R. Cao, *Angew. Chem., Int. Ed.* **2020**, *59*, 23641.

[56] A. Herzog, A. Bergmann, H. S. Jeon, J. Timoshenko, S. Kuhl, C. Rettenmaier, M. L. Luna, F. T. Haase, B. Roldan Cuenya, *Angew. Chem., Int. Ed.* **2021**, *60*, 7426.

[57] G. Silversmit, H. Poelman, V. Balcaen, P. M. Heynderickx, M. Olea, S. Nikitenko, W. Bras, P. F. Smet, D. Poelman, R. De Gryse, M.-F. Reniers, G. B. Marin, *J. Phys. Chem. Solids* **2009**, *70*, 1274.

[58] Y. Peng, Q. Liu, B. Lu, T. He, F. Nichols, X. Hu, T. Huang, G. Huang, L. Guzman, Y. Ping, S. Chen, *ACS Catal.* **2021**, *11*, 1179.

[59] H. Weller, *Angew. Chem., Int. Ed.* **1993**, *32*, 41.

[60] J. Liu, W. Cheng, Y. Wang, X. Fan, J. Shen, H. Liu, A. Wang, A. Hui, F. Nichols, S. Chen, *ACS Appl. Nano Mater.* **2021**, *4*, 4361.

[61] G. Chata, F. Nichols, R. Mercado, T. Assafa, G. L. Millhauser, C. Saltikov, S. Chen, *ACS Appl. Bio Mater.* **2021**, *4*, 7025.

[62] J.-L. Clement, N. Ferre, D. Siri, H. Karoui, A. Rockenbauer, P. Tordo, *J. Org. Chem.* **2005**, *70*, 1198.

[63] F. Nichols, K. I. Ozoemena, S. Chen, *Chin. J. Catal.* **2022**, *43*, 1399.

[64] E. M. Flores, M. L. Moreira, M. J. Piotrowski, *J. Phys. Chem. A* **2020**, *124*, 3778.

[65] J. Guo, J. Zhou, Z. Sun, M. Wang, X. Zou, H. Mao, F. Yan, *Acta Biomater.* **2022**, *146*, 370.

[66] K. Liu, Y. Song, S. Chen, *J. Power Sources* **2014**, *268*, 469.

[67] K. Liu, Y. Song, S. Chen, *Int. J. Hydrogen Energy* **2016**, *41*, 1559.

[68] Y. Peng, W. Pan, N. Wang, J.-E. Lu, S. Chen, *ChemSusChem* **2018**, *11*, 130.

[69] X. Jiang, W. He, X. Zhang, Y. Wu, Q. Zhang, G. Cao, H. Zhang, J. Zheng, T. R. Croley, J.-J. Yin, *J. Phys. Chem. C* **2018**, *122*, 29414.

[70] H. Guo, C.-G. Niu, C.-Y. Feng, C. Liang, L. Zhang, X.-J. Wen, Y. Yang, H.-Y. Liu, L. Li, L.-S. Lin, *Chem. Eng. J.* **2020**, *385*, 123919.